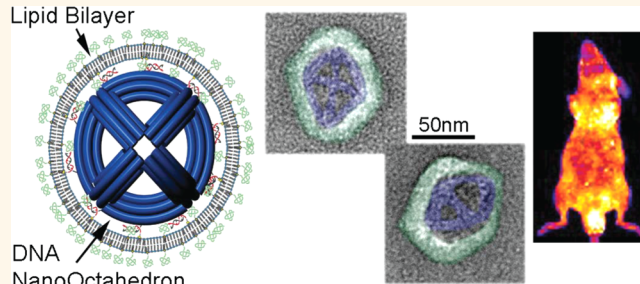


Virus-Inspired Membrane Encapsulation of DNA Nanostructures To Achieve *In Vivo* Stability

Steven D. Perrault^{†,‡} and William M. Shih^{†,‡,§,*}

[†]Wyss Institute for Biologically Inspired Engineering and [‡]Biological Chemistry and Molecular Pharmacology, Harvard Medical School, Boston, Massachusetts 02115, United States, and [§]Department of Cancer Biology, Dana Farber Cancer Institute, Boston, Massachusetts 02115, United States

ABSTRACT DNA nanotechnology enables engineering of molecular-scale devices with exquisite control over geometry and site-specific functionalization. This capability promises compelling advantages in advancing nanomedicine; nevertheless, instability in biological environments and innate immune activation remain as obstacles for *in vivo* application. Natural particle systems (*i.e.*, viruses) have evolved mechanisms to maintain structural integrity and avoid immune recognition during infection, including encapsulation of their genome and protein capsid shell in a lipid envelope. Here



we introduce virus-inspired enveloped DNA nanostructures as a design strategy for biomedical applications. Achieving a high yield of tightly wrapped unilamellar nanostructures, mimicking the morphology of enveloped virus particles, required precise control over the density of attached lipid conjugates and was achieved at 1 per $\sim 180 \text{ nm}^2$. Envelopment of DNA nanostructures in PEGylated lipid bilayers conferred protection against nuclease digestion. Immune activation was decreased 2 orders of magnitude below controls, and pharmacokinetic bioavailability improved by a factor of 17. By establishing a design strategy suitable for biomedical applications, we have provided a platform for the engineering of sophisticated, translation-ready DNA nanodevices.

KEYWORDS: DNA · nanotechnology · lipid bilayer · *in vivo* · nanostructure · imaging · immune · pharmacokinetics · biodistribution · PEG

Biomaterial nanotechnology has undergone considerable progress over the past five decades, from an initial demonstration of liposomes^{1,2} to that of a logic-gated nanorobot.³ Much of this development has focused on improving the detection and treatment of cancer by increasing the bioavailability and targeting specificity of anticancer agents.^{4–11} The rapidly growing field of structural DNA nanotechnology^{12–16} could advance these aims by expanding the range of available nanoparticle geometries and improving the precision of ligand functionalization, two key design parameters. Even more exciting is DNA nanotechnology's potential for engineering of highly sophisticated nanoscale devices. Recent studies include the nanorobot,³ programmable immuno-adjuvants,^{17,18} a synthetic membrane channel,¹⁹ and a molecular cascade capable of autonomously processing multiple inputs to determine cell phenotype.²⁰ Translation

of such devices into biomedical applications requires molecular engineers to first address the susceptibility of DNA nanostructures to nuclease degradation,²¹ as well as their ability to activate an inflammatory immune response.^{17,22} Inspired by the stability provided to enveloped viruses *via* their lipid membranes, we developed enveloped DNA nanostructures that address the above challenges (Figure 1a).

RESULTS AND DISCUSSION

To mimic the geometry of a viral protein capsid shell, we designed a wireframe DNA nano-octahedron (DNO) with an estimated diameter of $\sim 50 \text{ nm}$ (Supporting Information Figure 1).²³ The octahedron struts are each composed of a bundle of six $\sim 28 \text{ nm}$ long double helices^{14,24} engineered with a $\sim 90^\circ$ curvature (see Supporting Information Note 1).¹⁵ DNOs were self-assembled in a one-pot reaction by combining phage-derived scaffold DNA (p7308)²⁵ with 144

* Address correspondence to William_Shih@dfci.harvard.edu.

Received for review February 28, 2014 and accepted April 2, 2014.

Published online April 02, 2014
10.1021/nn5011914

© 2014 American Chemical Society

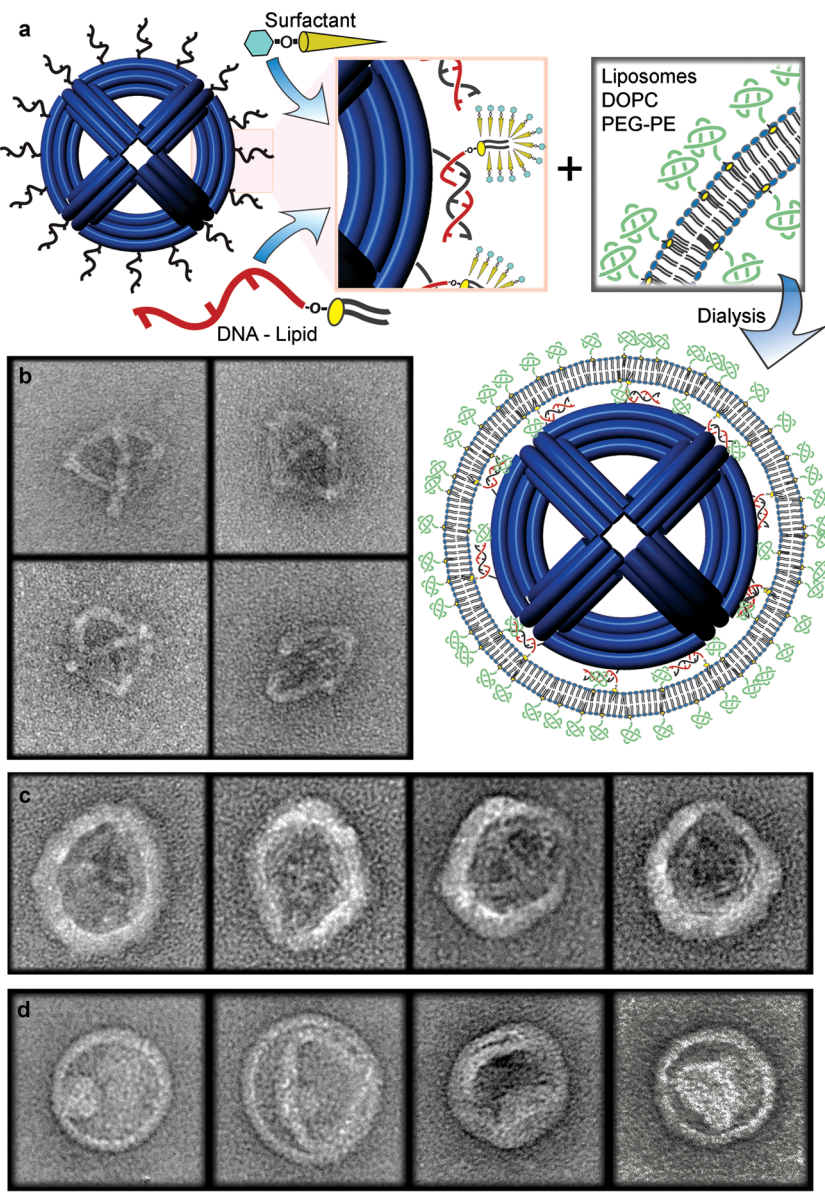


Figure 1. Schematic of the encapsulation strategy and negative-stain TEM. (a) Lipid–DNA conjugates are annealed to outer handles of non-encapsulated DNA nano-octahedron (N-DNO) in a surfactant solution that forms micelles around the conjugates. Liposomes are added, resulting in mixed surfactant–lipid micelles. Dialysis selectively removes the surfactant and results in a fused lipid bilayer around the DNO. (b) TEM images of purified N-DNO, (c) E-DNO, showing a tightly wrapped unilamellar membrane around the nanostructures, and (d) phi12 bacteriophage, showing comparable ultrastructure and dimensions to E-DNO (scale bar = 50 nm).

oligonucleotide staple strands (see Supporting Information Table 1) in a 15 h thermal annealing ramp. Correctly folded structures were isolated by glycerol-gradient centrifugation²⁶ and verified by negative-stain transmission electron microscopy (TEM) (Figure 1b and Supporting Information Figure 2).

Functional molecular features coupled to oligonucleotides can be assembled onto DNA nanostructures with high precision through hybridization to single-stranded DNA “handles” designed into the nanostructure. We designed an “inner” set of 12 identical handles (protruding from the inside face of the DNO struts) for attachment of fluorophore-conjugated

oligonucleotides, providing optical contrast agent functionality. We designed a second “outer” set of 48 handles (protruding from the outside face) for attachment of lipid-conjugated oligonucleotides²⁷ with the lipid positioned ~5 nm (2 nm 6-thymidine spacer + 2.5 nm double helix width + 0.5 nm linker for lipid) from the nanostructure frame to drive tight wrapping of the membrane around the structure.

Our encapsulation strategy involves directing lipid bilayer assembly around DNO, recruited by individual lipid-conjugated oligonucleotides preassembled onto outer handles. The lipid bilayers are reconstituted out of a solution of mixed lipid and surfactant

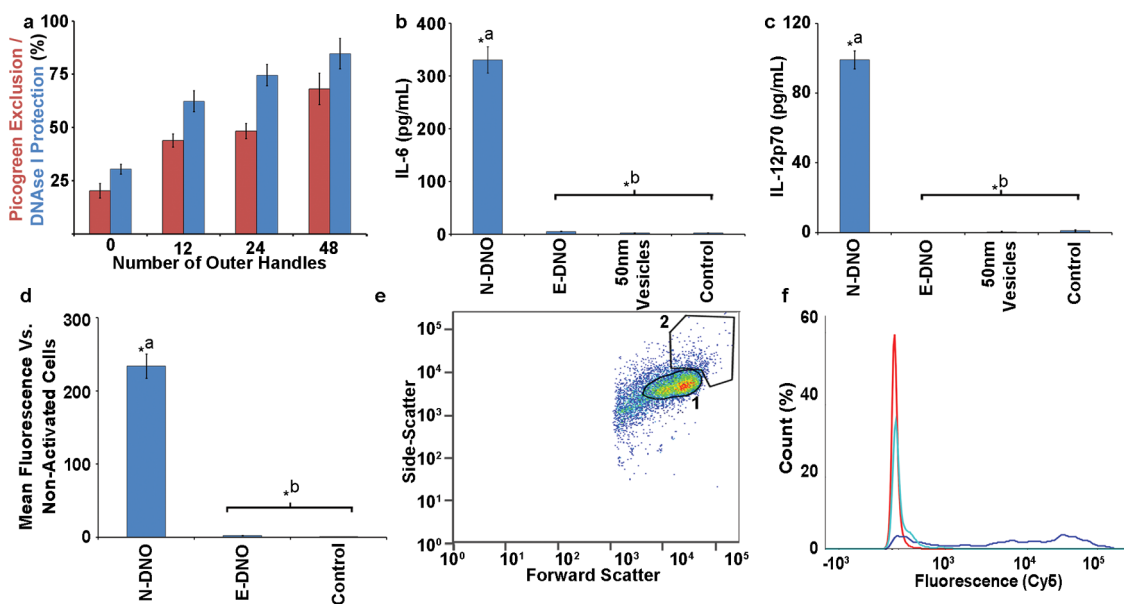


Figure 2. Bulk encapsulation yield and *in vitro* immune activation. (a) Encapsulation yield of outer handle DNO variants was estimated by PicoGreen dye membrane exclusion (red), and protection from nuclease was assayed with DNase I (blue). ELISA assay measurements of (b) IL-6 and (c) IL-12 cytokine production by splenocytes after incubation with N-DNO, E-DNO, and 50 nm vesicles for 16 h, as well as nonactivated controls. (d) Flow cytometry measurement of splenocyte mean fluorescence after incubation with Cy5-labeled N-DNO, E-DNO, and negative control. (e) Flow cytometry forward- (cell size) and side-scattering (granularity) properties of splenocytes was used to define two populations. Small, low granularity cells (1) were analyzed separately from large, high granularity cells (2). (f) Histogram of population (2) fluorescence after incubation with Cy5-labeled N-DNO (purple), E-DNO (blue), and negative controls (red). (*a,b: $p < 0.05$, ANOVA + Dunnet's test vs control, error bars indicate SEM).

(*N*-octyl- β -D-glucopyranoside) through a dialysis step that selectively removes the surfactant²⁸ to achieve the desired encapsulated DNO (E-DNO) (Figure 1c). We refer to DNO that has not been treated with lipids as non-encapsulated DNO (N-DNO). Unless otherwise stated, our membrane formulation includes 1,2-dioleoyl-sn-glycero-3-phosphocholine (DOPC) (94.2% molar contribution), 1,2-dioleoyl-sn-glycero-3-phosphoethanolamine-N-[methoxy(polyethylene glycol)-2000] (PEG-DOPE) (5%), and fluorescent rhodamine-1,2-dioleoyl-sn-glycero-3-phosphoethanolamine (Rh-DOPE) (0.8%).

We measured internalized DNO diameters of 53 nm versus outer membrane diameters of 76 ± 4 nm from TEM images of E-DNO (Supporting Information Figure 3). Our membrane formulation has an estimated thickness of ~ 4 nm lipid bilayer plus ~ 5 nm of PEG on each leaflet; therefore, the observed differential of ~ 12 nm per vesicle side is consistent with a unilamellar envelope. As anticipated based on our design inspiration, the ultrastructure and dimensions of E-DNO are similar to enveloped virus particles (e.g., phi12 bacteriophage, Figure 1d)²⁹ with our nanostructure taking the place of the protein capsid shell, wrapped tightly by a single lipid bilayer.

To optimize our bilayer reconstitution strategy, we synthesized additional variants of DNO having 0, 12, or 24 outer handles. After subjecting these to the lipid treatment described above, we examined the extent of association between nanostructures and vesicles using a membrane-impermeable DNA dye (PicoGreen).

Fluorescence-based quantification of DNO before and after membrane destabilization with surfactant revealed a direct correlation between outer handle number and the percent of nanostructures inaccessible to the dye (Figure 2a). We observed $20.2 \pm 3.5\%$ (\pm SEM) of the 0 handle variant was membrane-enclosed, suggesting there is a nonspecific interaction between the DNA and lipids. This could be tuned by addition of negatively charged lipid (15% 1,2-dioleoyl-sn-glycero-3-phospho-L-serine) to the membrane formulation, which decreased the nonspecific interaction to $5.1 \pm 2.7\%$ (Supporting Information Figure 4). The variant with 12 outer handles at an average density of ~ 1 handle per 710 nm^2 of nanostructure surface (surface area is defined as that of a sphere enclosing the DNO) showed $43.9 \pm 3.1\%$ membrane-enclosed. A comparable $48.3 \pm 3.5\%$ was measured with 24 handles (1 handle per $\sim 350 \text{ nm}^2$). The association between DNO and membranes was strongest with our design maximum of 48 outer handles (1 handle per $180 \text{ nm}^2/\text{handle}$), which showed $68.1 \pm 7.3\%$ enclosed within membranes.

We then tested protection from nuclease activity via DNase I digestion (Figure 2a). Following lipid treatment, 1.5 μg of each variant was incubated with 20 units of enzyme for 24 h at 37°C , and total remaining DNA was quantified by PicoGreen fluorescence and compared to non-nuclease-treated controls. The 0 outer handle sample showed little protection with $30.4 \pm 2.3\%$ DNA remaining, whereas $84.6 \pm 7.2\%$ remained in the 48 outer handle sample, clearly

showing that the envelope provides protection against nuclease digestion.

Negative-stain TEM revealed a far more dramatic impact of handle number on ultrastructure (Supporting Information Figure 5). Whereas most 0 handle DNOs were not associated with vesicles, those with 12 or 24 outer handles had much of their surface covered by vesicles formed external to the nanostructure frame. Imaging of 48 handle DNO revealed nanostructures within apparently complete and tightly associated lipid bilayers, as shown in Figure 1c. The number and density of attached lipid-conjugated oligonucleotides is therefore a key design parameter for DNO encapsulation. Successful encapsulation was also dependent on the liposome formulation. Removal of PEG-DOPE resulted in much larger reconstituted vesicles and no tightly wrapped nanostructures, suggesting that PEG plays an important role in controlling the extent of micelle fusion. We observed that cholesterol (~5%) can be used in place of PEG-DOPE to similarly control micelle fusion and to produce E-DNO (data not shown). Inclusion of both PEG (5%) and cholesterol (15%) caused stabilization of reconstituted vesicles at smaller diameters, suggesting an inhibition of fusion and trapping of a putative intermediate of the encapsulation process (Supporting Information Figure 6).

We next used density equilibrium centrifugation in an iodixanol gradient to separate 48 outer handle E-DNO from excess lipid vesicles, resulting in a highly enriched population (Supporting Information Figure 7). The final recovery yield of E-DNO relative to starting number of DNO used in encapsulation and the fraction of fully encapsulated nanostructures were determined by Picogreen quantification and membrane exclusion to be ~20 and 90%, respectively. This yield allowed us to prepare quantities of E-DNO suitable for *in vitro* and *in vivo* studies.

A significant innate inflammatory response would be a serious impediment to many biomedical applications of DNA nanotechnology. As a gauge of this, we incubated Cy-5-labeled N- and E-DNO, as well as empty 50 nm vesicles, with immune cells isolated from mouse spleens. Similar to previously reported results,^{17,18} N-DNO activated a potent inflammatory cytokine response comparable to that produced from exposure to bacterial or viral nucleic acids. Interleukin-6 (IL-6) and IL-12 were produced at 136 ± 10 - and 99 ± 5 -fold above nonactivated cells (Figure 2b,c). In contrast, E-DNO and 50 nm vesicles induced 2.1 ± 0.3 - and 0.9 ± 0.3 -fold increases, respectively, in IL-6 production *versus* controls. Similarly, IL-12 was undetectable after incubation with E-DNO and vesicles. Flow cytometry showed that mean fluorescence of splenocytes incubated with N-DNO was 111 ± 8 -fold higher than with E-DNO, which was equivalent to negative control cells (Figure 2d). N-DNO uptake was concentrated in a subpopulation of large, granular cells (Figure 2e,f) in which $89.0 \pm 3.2\%$ displayed very bright Cy5 signal. This

same subpopulation showed low mean fluorescence and few positive cells ($8.0 \pm 2.3\%$) after incubation with E-DNO, a result that was confirmed by confocal microscopy (Supporting Information Figure 8). This splenocyte assay shows that nanostructure activation of, and uptake by, immune cells can be almost fully attenuated by encapsulation in a PEGylated lipid membrane.

Encouraged by this, we next aimed to characterize the *in vivo* pharmacokinetics of E-DNO. AlexaFluor750-labeled oligonucleotides, N-DNO, and E-DNO were intravenously injected into anaesthetized mice to allow tracking *via* whole animal optical imaging for 120 min postinjection. Elimination half-life of the oligonucleotide control was estimated to be 38.0 ± 0.8 min, with signal rapidly accumulating in the bladder immediately after injection (Figure 3a,b). The half-life (49.5 ± 1.0 min) and clearance pattern of N-DNO were equivalent to the that of the oligonucleotide. Because nanoparticles larger than 6 nm are size-excluded from renal clearance,³⁰ these data indicate that the structural integrity of N-DNO becomes compromised immediately after injection. In contrast, E-DNO displayed an estimated half-life of 370 ± 38 min (Figure 3c), comparable to similarly formulated PEGylated liposomes,⁴ with little bladder accumulation. In comparison to N-DNO, encapsulation increased the elimination half-life and relative bioavailability by factors of 9 and 17, respectively.

The stability of DNA nanostructures and devices has previously been probed during exposure to lysate from sodium dodecyl sulfate-treated mammalian cells,³¹ and after direct injection into *Caenorhabditis elegans*,³² with little degradation observed. Comparison to our findings is confounded by the presence of nuclease-inhibiting surfactant, distinct nanostructure designs, and an alternative *in vivo* model system, yet the observed differences suggest that DNA-based nanomaterials may be sensitive to their environment in a design-dependent manner. A folate-targeted, DNA-based nanoparticle was also recently tested in a murine tumor model,³³ displaying an elimination half-life (24.2 min) and kidney uptake similar to our non-encapsulated DNO, suggesting it may have suffered from a comparable, rapid degradation profile after injection.

Finally, we profiled biodistribution by imaging organs harvested 120 min postinjection (Figure 3d,e). No significant differences were observed between the distribution profiles of oligonucleotide and N-DNO on an organ-by-organ basis, and both displayed significant renal excretion with signal in urine of 86.3 ± 3.6 and $88.5 \pm 2.9\%$ (% of total, photons/g), respectively. In contrast, E-DNO urine accumulation reached only $11.0 \pm 4.4\%$ of AlexaFluor750 signal at this time point, while maintaining $85.0 \pm 4.4\%$ in blood. Dual labeling of the E-DNO membrane (rhodamine) and DNA nanostructure (AlexaFluor750) allowed us to compare biodistribution of both components through multiplex imaging (Supporting Information Figure 9).

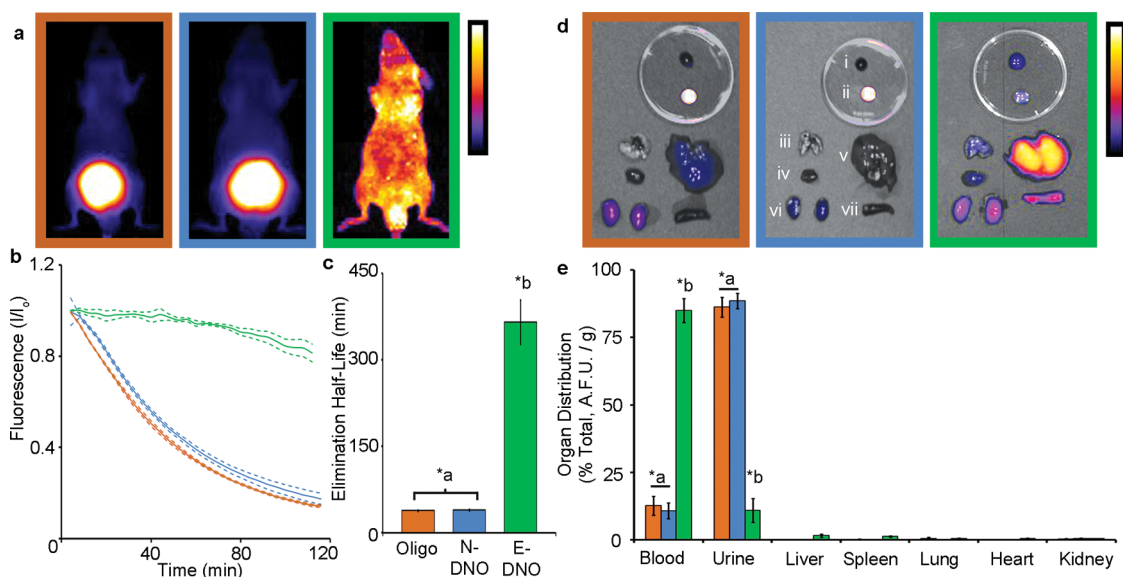


Figure 3. *In vivo* optical imaging for analysis of pharmacokinetics and biodistribution. Mice were injected with AlexaFluor750-labeled oligonucleotide (orange), N-DNO (blue), or E-DNO dual-labeled with rh-DOPE (green) and imaged for 120 min postinjection. (a) Fluorescence images of mice at 120 min postinjection. E-DNO is seen throughout the body, whereas the other two agents have accumulated in the bladder (calibration bar = 500–20000 afu). (b) Mean fluorescence (measured in a region-of-interest traced around the head and torso) vs time, relative to the signal at $t = 8$ min (I/I_0). (c) Elimination half-lives estimated from the kinetic analysis. (d) Fluorescence images of organs harvested 120 min postinjection, shown overlaid with photographic images (i) blood, (ii) urine, (iii) lung, (iv) heart, (v) liver, (vi) kidneys, (vii) spleen, calibration bar = 1500–25000 afu). (e) Organ distribution of AlexaFluor750 fluorescence (% of total, afu/g after correcting for calculated blood volumes of organs). (*a,b $p < 0.05$, ANOVA + Tukey's test, dashed lines and error bars indicate SEM).

No significant differences were observed between the two components, suggesting that they remained associated throughout imaging.

As a last comparison, we examined the biodistribution of 50 nm liposomes of the same formulation, hydrodynamic diameter, and concentration as E-DNO (Extended Data Figure 9). No significant differences in rhodamine fluorescence were observed between the major organs. Yet surprisingly, the 50 nm liposomes cleared more rapidly than E-DNO, with twice as much signal ($38.0 \pm 3.2\%$ vs $20.1 \pm 4.3\%$, respectively) measured in urine. This was contrasted with $58.0 \pm 2.5\%$ and $76.2 \pm 3.3\%$ signal remaining in blood of liposome and E-DNO injected animals. Although it requires more in-depth follow-up studies, it would be interesting if DNO acts as a stabilizing endoskeleton and reduces clearance of liposomes.

CONCLUSIONS

This virus-inspired E-DNO displays favorable *in vitro* and *in vivo* properties, in stark contrast to non-enveloped DNO which activates a potent immune response and displays rapid degradation after injection. Using this design strategy as a starting point,

many different biomedical applications can be conceived through integration of additional functions. Because our E-DNO incorporates a contrast agent and has appropriate dimensions and pharmacokinetic properties, it could easily be adapted for tumor detection.⁵ Addition of ligands to the outer membrane leaflet would add specificity for target molecules or cells, and such ligands could potentially be spatially organized by the DNA “capsid shell” using transmembrane linkers. Many different triggers could be implemented to drive an internal molecular cascade or a mechanical reconfiguration of the nanostructure frame (e.g., photon-fuelled,³⁴ thermally³⁵ or chemically induced³⁶ conformational switch, pH-sensitive lipids³⁷), which could be used for contrast agent unmasking, drug release, or more sophisticated behaviors that have been difficult to achieve using conventional nanomaterials or multicomponent nanodevices.^{9–11} A more distant but highly exciting prospect is the development of autonomous devices having functions approaching that of virus particles (e.g., cell entry via attachment and fusion) or primitive immune cells (e.g., input-based therapeutic response), and which could provide significant advances in diagnostics and therapeutics.

METHODS

Reagents. Lipids DOPC and DOPS, and PEG-PE, cholesterol and rhodamine-PE, the mini-extruder, extrusion membranes, and accessories were purchased from Avanti Polar Lipids.

Endotoxin test cartridges (0.05–5.0 EU/mL) were purchased from Charles River. Accugene 10× TBE buffer, PCR tubes, and 96-well PCR plates (Axygen) were purchased from VWR. SYBR Safe and PicoGreen stains were purchased from Life

Technologies Corporation. Agarose and cell lysis buffer were purchased from Lonza. Glycerol, Tris base, EDTA, Triton X-114, octyl β -D-glucopyranoside (OG), Tween20, magnesium chloride, magnesium sulfate, sodium chloride, and paraformaldehyde were purchased from Sigma-Aldrich. RPMI, PBS, FBS, and penicillin-streptomycin were purchased from Gibco. Carbon Formvar grids and uranyl formate were purchased from Electron Microscopy Sciences. The 96- and 384-well fluorescence assay plates were purchased from BD Biosciences. Amicon Ultra filtration devices, Optiprep media, and Seton ultracentrifugation tubes were purchased from Fisher Scientific.

DNA Nanostructure Folding. The DNA nano-octahedron was designed using cadDNAo.²³ Staples strands were purchased reverse-phase-purified from Bioneer or Life Technologies Corporation. Fluor-coupled oligonucleotides were custom-synthesized and purified by IDT Technologies. The p7308 scaffold strand was produced from m13 phage replication in *Escherichia coli*, as described previously.²⁵

The scaffold strand was endotoxin-purified using Triton X-114. In brief, surfactant was added to scaffold stock to a final concentration of 2% (v/v) and incubated at 4 °C on an inversion mixer for 30 min. The solution was mixed at 37 °C for 5 min to cause phase separation, then centrifuged at 37 °C for 30 min at maximum speed in a benchtop centrifuge. The upper aqueous fraction was transferred to a new tube. This was repeated four times to reduce endotoxin in the scaffold stock solution to acceptable levels of less than 5 EU/mL, quantified using the Endosafe-PTS system and test cartridges (Charles River). Downstream DNA nanostructure purification and dilution steps reduced endotoxin to undetectable levels prior to *in vitro* tissue culture and *in vivo* imaging experiments.

Folding was tested over a range of MgCl₂ concentrations. A solution of 10 nM scaffold was mixed with a 5-fold molar excess of each of 144 staples strands in 5 mM Tris (pH 8.0), 1 mM EDTA (1× TE), and 10–22 mM MgCl₂. The solution was then subjected to a thermal annealing ramp on a Tetrad 2 Peltier thermal cycler (Bio-Rad) according to the following schedule:

80 °C for 5 min
decrease to 65 °C at 5 min/°C
incubate at 65 °C for 20 min
decrease to 25 °C at 20 min/°C

The products were separated in a 1.5% agarose gel + 10 mM MgCl₂ and SYBR Safe stain, in 0.5× TBE buffer + 10 mM MgCl₂, for 3 h at 60 V. The leading bands were extracted and imaged by TEM. We opted for a 14 mM MgCl₂ concentration for the synthesis of stock DNA nanostructures.

Negative-Stain Transmission Electron Microscopy. TEM imaging was carried out by dropping 3.5 μ L of product onto a plasma-treated carbon Formvar grid. This was incubated for 1 min, wicked away onto filter paper, 3.5 μ L of 2% uranyl formate (in H₂O, w/v) was added for 30 s, then wicked away. Imaging was carried out on a JEOL 1400 transmission electron microscope.

Purification of Synthesized Nanostructures. Solutions of folded DNA nanostructures were concentrated and then purified by glycerol gradient ultracentrifugation, as described elsewhere.²⁶

Liposome Preparation. Liposomes were prepared using standard techniques. We produced a mixture of DOPC, PEG2K-PE, and rhodamine-PE (molar ratio 94.2, 5.0, 0.8), or DOPC, DOPS, PEG2K-PE, and rhodamine-PE (79.2:15.5:0.8), or DOPC, cholesterol, PEG2K-PE, and rhodamine-PE (79.2, 15.0, 5.0, 0.8) in chloroform in a glass tube. Chloroform was evaporated using a dry N₂ line, and the film was placed under vacuum overnight. We added a volume of encapsulation buffer (5 mM Tris-HCl, 1 mM EDTA, 10 mM MgCl₂, 10 mM NaCl) to the film. Typically, we would add 300 μ L of buffer to a total of 4.5 μ mol of lipid. The film was resuspended by shaking on a Thermomixer (Eppendorf) at 850 rpm, room temperature for 1 h. The solution was then put through seven rounds of freezing and thawing by passing between liquid N₂ and a room temperature water bath, then extruded with 21 passes through a Mini-Extruder (Avanti Polar Lipids) and a 0.2 μ m polycarbonate membrane. Liposomes were stored at 4 °C, light-protected for up to 4 weeks.

The 50 nm empty vesicles prepared for *in vitro* and *in vivo* experiments were prepared in the same manner, except with a

50 nm extrusion membrane after extrusion through the 200 nm membrane.

Lipid–DNA Conjugate. The lipid–DNA conjugate was synthesized as described elsewhere.²⁷

DNA Nanostructure Encapsulation. In brief, DNA nanostructures were encapsulated by first annealing lipid–oligonucleotide and fluor–oligonucleotide conjugates to the nanostructure in a surfactant buffer. The annealed product was purified by glycerol gradient, then mixed with liposomes. This was then dialyzed to remove surfactant, and the product was purified, concentrated, dialyzed against a buffer appropriate to downstream experiments, and characterized. Sample volumes listed below were found to be scalable.

In a typical experiment, a 400 μ L solution was prepared, containing 20–200 μ g/mL DNO mixed with a 5× molar excess (relative to handle number) of lipid– and fluor–oligonucleotide conjugates in encapsulation buffer + 2% OG surfactant. The solution was incubated for a minimum of 2 h at 35 °C on a Tetrad 2 Peltier Cycler (Bio-Rad).

The annealed product was purified from excess lipid–DNA and fluor–DNA conjugates via glycerol gradients containing OG surfactant. Glycerol gradients were prepared using solutions of 15% glycerol + 2% OG and 45% glycerol + 2% OG in encapsulation buffer.²⁶ The annealed product was layered on top of the gradients and centrifuged for 2.5 h at 41 000 rpm (for SW-41 rotor tubes). The gradients were then fractionated, and appropriate fractions were combined and concentrated back to the starting volume (*i.e.*, 400 μ L) using an Amicon 30K device.

The concentration of the product was determined by UV absorbance at 260 nm on a Nanodrop system with disposable cuvettes. The volume was transferred into a 2.0 mL microcentrifuge tube. Liposomes were added by transferring a 0.5× volume of prepared liposomes into the solution (*i.e.*, 200 μ L). This was mixed on the Thermomixer at 450 rpm, room temperature for 1 h. A volume of encapsulation buffer equivalent to the current total volume (*i.e.*, 600 μ L) was added and mixed gently. The entire solution was then transferred into an appropriately sized 7K MWCO Slide-a-Lyzer dialysis cassette (Thermo Scientific). The cassette was floated in 2 L of encapsulation buffer for 3 days for small samples (*e.g.*, 120 μ L) or 7 days for large volumes (*e.g.*, 12 mL). Buffer was replaced every second day in all cases.

After dialysis, the sample was recovered from the dialysis cassette and concentrated using an Amicon column pretreated with encapsulation buffer.

Enveloped nanostructures were separated from excess lipids by equilibrium centrifugation using iodixanol (Optiprep reagent, Sigma-Aldrich). We prepared a working volume of 54% iodixanol from the stock 60% solution by mixing with 0.1× volume of 10× encapsulation buffer. We then mixed the 54% Iodixanol/Encapsulation Buffer solution with 1x Encapsulation Buffer to prepare equal volumes of 35, 28, 18, and 8% iodixanol/encapsulation buffer. In the case of the 35% step, the encapsulated DNA nanostructure sample was used in place of 1x encapsulation buffer to dilute the 54% iodixanol solution. The volumes were layered into ultracentrifuge tubes and centrifuged at maximum allowable speed for 16 h, 4 °C. The gradient was fractionated, and 50 μ L of each fraction was transferred into a 96-well fluorescence plate (BD Bioscience) and imaged on the Typhoon system (GE Healthcare Life Sciences). The fractionation was profiled by quantifying fluorescent signals in each fraction using ImageJ (NIH). The images were background-subtracted, then a circular region-of-interest (ROI) was placed over each well, and integrated density was measured. The integrated density values were plotted against fraction number to profile component distribution. Appropriate fractions containing E-DNO (based on Cy5 or AlexaFluor750 signal) were concentrated and washed with encapsulation buffer using an Amicon centrifugation filter device or, in some cases, were first dialyzed against a buffer appropriate for downstream experiments (*e.g.*, phosphate-buffered saline, Gibco).

The encapsulated, purified products were characterized by TEM, DLS, and fluorescence, and the encapsulation yield was determined by a PicoGreen assay (described below). DLS was carried out on a Nano ZS (Malvern) using standard settings.

Fluorescence analysis was carried out on a Fluorolog (Horiba) using the following settings. For rhodamine fluorescence of vesicles, excitation was at 550 nm and emission scanned from 575 to 700 nm. For Cy5 nanostructure fluorescence, excitation was at 625 nm and emission scanned from 650 to 800 nm. For AlexaFluor750 fluorescence, excitation was at 700 nm and emission scanned at 725–900 nm.

PicoGreen Dye Exclusion Assay. The PicoGreen stain exclusion assay differentiates between membrane-enclosed and non-enclosed DNA based on the stain's inability to cross a lipid bilayer. Measurements are made in parallel in encapsulation buffer and buffer with OG that destabilizes the membrane and allows the stain access to total DNA content of a sample. The assay is carried out in a 384-well black fluorescence assay plate (Greiner).

A standard curve was first prepared from the DNA nanostructure stock solutions. First 200 μ L of 5 μ g/mL was prepared in encapsulation buffer, then 6 \times 1:2 dilutions were prepared from this. Next 100 μ L of each unknown sample was prepared by dilution with encapsulation buffer (typically 1:5–1:50), aiming for the concentration of the diluted sample to be within the standard curve range. Two solutions of PicoGreen stain were prepared by diluting the stock reagent 1:200 in either encapsulation buffer, or encapsulation buffer + 2% OG. For each standard or sample to be measured, 10 μ L of both PicoGreen solutions was pipetted into 3 \times wells of the 384-well plate. Ten microliters of the standards and samples was then added to the 6 \times wells, and the plate was incubated 5 min and light-protected. Fluorescence of the PicoGreen stain was measured on a SpectraMax M5 plate reader (Molecular Devices) by excitation/emission at 480/520 nm.

For analysis, standard curves were plotted for median fluorescence values of both the OG-negative and OG-positive buffers. These were used to calculate the DNA concentration of unknown samples in the two buffers. The concentration of DNA in the OG-containing buffer equals "total DNA", whereas that in the encapsulation buffer was "non-encapsulated DNA". Encapsulation yield is then calculated by

$$\text{(total DNA} - \text{non-encapsulated DNA})/\text{total DNA} \times 100\%$$

Nuclease Protection Assay. Sensitivity to nuclease activity was determined using DNase I (New England Biolabs). The encapsulation process was carried out on 0, 12, 24, and 48 outer handle DNA nanostructure variants at a point prior to purification by float-up centrifugation. One hundred microliters of each was transferred into PCR tubes ($n = 3$ for DNase I-positive and DNase I-negative of each variant, 12 tubes in total). Ten units of DNase I were added to 3 \times replicates of each variant, and an equivalent volume of DNase I buffer was added to 3 \times replicates as negative controls. All samples were incubated for 24 h at 37 °C on a Tetrad 2 Peltier thermocycler. Following this, the PicoGreen assay was used to determine the DNA remaining after nuclease digestion. The percent remaining was expressed as a ratio of the calculated DNA remaining in the DNase I-positive samples over the DNase I-negative samples for each design.

Splenocyte Activation Assay. RPMI media (Gibco) used for splenocyte tissue culture were adjusted to maintain the stability of DNA nanostructures. Mg²⁺ was adjusted to 6 mM by addition of MgSO₄, diluting the media with sterile ultrapure H₂O to maintain osmolarity. Cell viability and cytokine response in this medium was validated prior to data collection. To heat-inactivate nuclease activity present in FBS, serum was heat-treated for 2 min at 75 °C in 1 mL volumes on a Thermomixer at 1000 rpm. Heat-inactivated serum was added to RPMI at 10%. Penicillin-streptomycin (Gibco) was added at an appropriate dilution.

Spleens were obtained from female 8 week old C57Bl/6 mice (Charles River). Two spleens were processed for each experiment. They were transferred into 70 μ m cell strainers (BD Falcon) and were dissociated using a sterile syringe plunger. The single cell suspension was washed through the cell strainer with 25 mL of PBS (Gibco) into a Petri dish. The suspension was transferred to a 50 mL Falcon tube, and PBS was added to a total volume of 40 mL. This was centrifuged at 500g for 5 min, and the supernatant was removed and discarded. PBS (40 mL) was

added, the pellet was resuspended to wash the cells and dilute nuclease enzymes, and the sample was resuspended. A total of 3 \times washes were used to remove nuclease activity carried over from the tissue. Two milliliters of ACK lysing buffer (Lonza) was added, and the cells were gently resuspended and incubated for 7 min. Following this, 20 mL of PBS and 20 mL of RPMI media were added, and the suspension was centrifuged as above. The supernatant was discarded, and 15 mL of RPMI media was added. After sitting for several minutes to allow settling of large cell and tissue aggregates, the upper 10 mL of suspension was transferred to a new 15 mL Falcon tube.

Cell concentration was determined, and 1 \times 10⁶ live cells were transferred in 450 μ L to 4 \times wells of a 48-well plate for each sample to be assayed. Then, 50 μ g/mL solutions of Cy5-labeled N- and Cy5-/rhodamine E-DNO were prepared (quantification via PicoGreen). A solution of 50 nm vesicles was prepared, with a concentration equivalent to E-DNO based on rhodamine absorbance. Fifty microliters of the nanostructure or vesicle samples was transferred into the wells ($n = 4$). These were incubated for 16 h in a CO₂ incubator at 37 °C. Supernatants were removed and centrifuged for 10 min at 500g, transferred to new tubes, and assayed for cytokine expression immediately or stored at –80 °C.

Cytokine concentrations were determined by enzyme-linked immunosorbent assays (R&D Systems) following the protocols exactly.

Flow Cytometry. Cell pellets from the above splenocyte experiment were fixed by addition of 1.0 mL of 4% paraformaldehyde/PBS solution for 15 min. Cell samples were pelleted and washed 1 \times with PBS, then resuspended in 500 μ L of PBS. Flow cytometry was carried out on a LSRFortessa (BD) using a 640 nm laser line with 670/30 nm emission filter to determine Cy5 fluorescence in samples (10000 events/measurement, $n = 4$). Gating was performed on splenocytes and "granulocytes" (large, granular cell population) by gating upon the FSC versus SSC dot plot. Identical gates were applied to all samples. After gating, a negative population was defined using the histogram obtained for media-only negative control samples. Samples that showed a rightward peak shift were determined as positive. Gates were applied to Cy5 histograms for splenocytes and granulocytes.

Confocal Imaging. Confocal imaging was carried out on splenocytes obtained from the above assay. The splenocytes were stained with a 20 mM Hoechst 33342 solution for 20 min, then resuspended in PBS. Cells were transferred into glass bottom dishes for imaging of Cy5 and Hoechst staining using standard filter sets and methods on an SP5 xMP inverted confocal microscope (Leica). All images were acquired with a 63 \times 1.2 water objective, 405 diode laser (Hoechst) and white light laser tuned to 575 nm (Alexa 568). Emission was collected with Leica Hybrid Detectors from 415 to 550 nm for Hoechst and 585–795 nm for Alexa 568. Optical zoom was used for higher magnification image.

In Vivo Optical Imaging. Optical imaging experiments were carried out on an IVIS Spectrum instrument (PerkinElmer). Athymic C57 nude mice (Charles River) were anaesthetized under 3% isoflurane and were then injected via tail vein with a 100 μ L bolus of AlexaFluor750-labeled (AF750) N-DNO, AF750/rhodamine-labeled E-DNO at 50 nM, or rhodamine-labeled 50 nm liposomes of the same formulation used for encapsulation. They were immediately transferred to the imaging system, and data collection was initiated. Animals were maintained at 2% isoflurane throughout imaging. Fluorescence images for kinetic analysis were acquired by a 30 s excitation at 745 nm and emission at 800 nm, every 4 min for a total of 30 images over 120 min postinjection.

Following collection of kinetic data, mice were immediately euthanized and blood was collected by cardiac puncture and transferred into heparin collection tubes. Urine and organs were harvested and were imaged on the IVIS system for 2 s at 570/620 nm (rhodamine) or 30 s at 745/800 nm (AF750).

Analysis was carried out in ImageJ. In all cases, images were background-subtracted using a 50 pixel rolling ball radius. Pharmacokinetic analysis was carried out using the Freehand Selection tool to draw a ROI around the complete head and

torso of the animal to just below the front legs. The integrated density was measured in each image. The data set was normalized to the value at 8 min postinjection, as this showed peak fluorescence after diffusion of the agents throughout the vascular system. Organ measurements were obtained using the Freehand Selection tool to draw ROI around their perimeter and measuring integrated density. Fifty microliter volumes of blood and urine were measured. "Organ distribution" was calculated for each organ as a percent of the total measured arbitrary fluorescent units, with urine normalized to a 200 μL estimated bladder volume and blood to 2500 μL estimated total blood volume. The contribution of organ fluorescence from blood volume³⁸ was calculated and subtracted from total fluorescence.

Statistics. Student's *t* test and ANOVA with posthoc Dunnett's or Tukey's tests were performed using an excel plug-in, iner-STAT-a v1.3 by Mario H. Vargas (Instituto Nacional de Enfermedad Respiratorias, Mexico).

Animal Use. All animal studies were performed in accordance with NIH guidelines, under approval of Harvard University's Institutional Animal Care and Use Committee.

Conflict of Interest: The authors declare the following competing financial interest(s): We filed a provisional patent on this technology.

Acknowledgment. We thank Dr. James Rothman and Jing Wang for their contribution of the oligonucleotide–lipid conjugate, Dr. Paul Gottlieb for his contribution of phi12 bacteriophage, Thomas Ferrante, Amanda Graveline, and Garry Cuneo for technical support, and Dr. Chenxiang Lin for discussions. S.D.P. holds a Canadian Institutes of Health Research Fellowship and a Wyss Institute Technology Development Fellowship, and this work was supported by NIH Grant 1DP2OD004641 and ARO MURI Grant W911NF-12-1-0420 to W.M.S., and by the Wyss Institute at Harvard.

Supporting Information Available: Methods, additional data, and a nanostructure design schematic and oligonucleotide sequences are available as Supporting Information. This material is available free of charge via the Internet at <http://pubs.acs.org>.

REFERENCES AND NOTES

- Glauert, A. M.; Dingle, J. T.; Lucy, J. A. Action of Saponin on Biological Cell Membranes. *Nature* **1962**, *196*, 953–955.
- Horne, R. W.; Bangham, A. D.; Whittaker, V. P. Negatively Stained Lipoprotein Membranes. *Nature* **1963**, *200*, 1340.
- Douglas, S. M.; Bachelet, I.; Church, G. M. A Logic-Gated Nanorobot for Targeted Transport of Molecular Payloads. *Science* **2012**, *335*, 831–834.
- Klibanov, A. L.; Maruyama, K.; Torchilin, V. P.; Huang, L. Amphiphatic Polyethyleneglycols Effectively Prolong the Circulation Time of Liposomes. *FEBS Lett.* **1990**, *268*, 235–237.
- Perrault, S. D.; Walkey, C.; Jennings, T.; Fischer, H. C.; Chan, W. C. W. Mediating Tumor Targeting Efficiency of Nanoparticles through Design. *Nano Lett.* **2009**, *9*, 1909–1915.
- Rodriguez, P. L.; Harada, T.; Christian, D. A.; Pantano, D. A.; Tsai, R. K.; Discher, D. E. Minimal "Self" Peptides That Inhibit Phagocytic Clearance and Enhance Delivery of Nanoparticles. *Science* **2013**, *339*, 971–975.
- Åkerman, M. E.; Chan, W. C. W.; Laakkonen, P.; Bhatia, S. N.; Ruoslahti, E. Nanocrystal Targeting *in Vivo*. *Proc. Natl. Acad. Sci. U.S.A.* **2002**, *99*, 12617–12621.
- Farokhzad, O.; Jon, S.; Khademhosseini, A.; Tran, T.; LaVan, D.; Langer, R. Nanoparticle–Aptamer Bioconjugates: A New Approach for Targeting Prostate Cancer Cells RID A-9435-2010. *Cancer Res.* **2004**, *64*, 7668–7672.
- Perrault, S. D.; Chan, W. C. W. *In Vivo* Assembly of Nanoparticle Components To Improve Targeted Cancer Imaging. *Proc. Natl. Acad. Sci. U.S.A.* **2010**, *107*, 11194–11199.
- Park, J.-H.; von Maltzahn, G.; Xu, M. J.; Fogal, V.; Kotamraju, V. R.; Ruoslahti, E.; Bhatia, S. N.; Sailor, M. J. Cooperative Nanomaterial System To Sensitize, Target, and Treat Tumors. *Proc. Natl. Acad. Sci. U.S.A.* **2010**, *107*, 981–986.
- Von Maltzahn, G.; Park, J.-H.; Lin, K. Y.; Singh, N.; Schwoeppel, C.; Mesters, R.; Berdel, W. E.; Ruoslahti, E.; Sailor, M. J.; Bhatia, S. N. Nanoparticles That Communicate *in Vivo* To Amplify Tumour Targeting. *Nat. Mater.* **2011**, *10*, 545–552.
- Seeman, N. C. Nanomaterials Based on DNA. *Annu. Rev. Biochem.* **2010**, *79*, 65–87.
- Rothenmund, P. W. K. Folding DNA To Create Nanoscale Shapes and Patterns. *Nature* **2006**, *440*, 297–302.
- Douglas, S. M.; Dietz, H.; Liedl, T.; Höglberg, B.; Graf, F.; Shih, W. M. Self-Assembly of DNA into Nanoscale Three-Dimensional Shapes. *Nature* **2009**, *459*, 414–418.
- Dietz, H.; Douglas, S. M.; Shih, W. M. Folding DNA into Twisted and Curved Nanoscale Shapes. *Science* **2009**, *325*, 725–730.
- Ke, Y.; Ong, L. L.; Shih, W. M.; Yin, P. Three-Dimensional Structures Self-Assembled from DNA Bricks. *Science* **2012**, *338*, 1177–1183.
- Schüller, V. J.; Heidegger, S.; Sandholzer, N.; Nickels, P. C.; Suhartha, N. A.; Endres, S.; Bourquin, C.; Liedl, T. Cellular Immunostimulation by CpG-Sequence-Coated DNA Origami Structures. *ACS Nano* **2011**, *5*, 9696–9702.
- Li, J.; Pei, H.; Zhu, B.; Liang, L.; Wei, M.; He, Y.; Chen, N.; Li, D.; Huang, Q.; Fan, C. Self-Assembled Multivalent DNA Nanostructures for Noninvasive Intracellular Delivery of Immunostimulatory CpG Oligonucleotides. *ACS Nano* **2011**, *5*, 8783–8789.
- Langecker, M.; Arnaut, V.; Martin, T. G.; List, J.; Renner, S.; Mayer, M.; Dietz, H.; Simmel, F. C. Synthetic Lipid Membrane Channels Formed by Designed DNA Nanostructures. *Science* **2012**, *338*, 932–936.
- Rudchenko, M.; Taylor, S.; Pallavi, P.; Dechkovskaya, A.; Khan, S.; Butler, V. P., Jr.; Rudchenko, S.; Stojanovic, M. N. Autonomous Molecular Cascades for Evaluation of Cell Surfaces. *Nat. Nanotechnol.* **2013**, *8*, 580–586.
- Nadano, D.; Yasuda, T.; Kishi, K. Measurement of Deoxyribonuclease I Activity in Human Tissues and Body Fluids by a Single Radial Enzyme-Diffusion Method. *Clin. Chem.* **1993**, *39*, 448–452.
- Kawai, T.; Akira, S. The Role of Pattern-Recognition Receptors in Innate Immunity: Update on Toll-like Receptors. *Nat. Immunol.* **2010**, *11*, 373–384.
- Douglas, S. M.; Marblestone, A. H.; Teerapittayanon, S.; Vazquez, A.; Church, G. M.; Shih, W. M. Rapid Prototyping of 3D DNA-Origami Shapes with caDNano. *Nucleic Acids Res.* **2009**, *37*, 5001–5006.
- Mathieu, F.; Liao, S.; Kopatsch, J.; Wang, T.; Mao, C.; Seeman, N. C. Six-Helix Bundles Designed from DNA. *Nano Lett.* **2005**, *5*, 661–665.
- Douglas, S. M.; Chou, J. J.; Shih, W. M. DNA-Nanotube-Induced Alignment of Membrane Proteins for NMR Structure Determination. *Proc. Natl. Acad. Sci. U.S.A.* **2007**, *104*, 6644–6648.
- Lin, C.; Perrault, S. D.; Kwak, M.; Graf, F.; Shih, W. M. Purification of DNA-Origami Nanostructures by Rate-Zonal Centrifugation. *Nucleic Acids Res.* **2013**, *41*, e40.
- Chan, Y. H.; Van Lengerich, B.; Boxer, S. G. Effects of Linker Sequences on Vesicle Fusion Mediated by Lipid-Anchored DNA Oligonucleotides. *Proc. Natl. Acad. Sci. U.S.A.* **2009**, *106*, 979–984.
- Ollivon, M.; Lesieur, S.; Grabielle-Madelenmont, C.; Paternostre, M. Vesicle Reconstitution from Lipid–Detergent Mixed Micelles. *Biochim. Biophys. Acta, Biomembr.* **2000**, *1508*, 34–50.
- Noda, T. Native Morphology of Influenza Virions. *Front. Virol.* **2012**, *2*, 269–273.
- Soo Choi, H.; Liu, W.; Misra, P.; Tanaka, E.; Zimmer, J. P.; Itty Ipe, B.; Bawendi, M. G.; Frangioni, J. V. Renal Clearance of Quantum Dots. *Nat. Biotechnol.* **2007**, *25*, 1165–1170.
- Mei, Q.; Wei, X.; Su, F.; Liu, Y.; Youngbull, C.; Johnson, R.; Lindsay, S.; Yan, H.; Meldrum, D. Stability of DNA Origami Nanoarrays in Cell Lysate. *Nano Lett.* **2011**, *11*, 1477–1482.
- Surana, S.; Bhatia, D.; Krishnan, Y. A Method To Study *In Vivo* Stability of DNA Nanostructures. *Methods* **2013**, *64*, 94–100.

33. Lee, H.; Lytton-Jean, A. K. R.; Chen, Y.; Love, K. T.; Park, A. I.; Karagiannis, E. D.; Sehgal, A.; Querbes, W.; Zurenko, C. S.; Jayaraman, M.; et al. Molecularly Self-Assembled Nucleic Acid Nanoparticles for Targeted *In Vivo* siRNA Delivery. *Nat. Nanotechnol.* **2012**, *7*, 389–393.
34. Liu, H.; Xu, Y.; Li, F.; Yang, Y.; Wang, W.; Song, Y.; Liu, D. Light-Driven Conformational Switch of I-Motif DNA. *Angew. Chem., Int. Ed.* **2007**, *46*, 2515–2517.
35. Juul, S.; Iacovelli, F.; Falconi, M.; Kragh, S. L.; Christensen, B.; Frøhlich, R.; Franch, O.; Kristoffersen, E. L.; Stougaard, M.; Leong, K. W.; et al. Temperature-Controlled Encapsulation and Release of an Active Enzyme in the Cavity of a Self-Assembled DNA Nanocage. *ACS Nano* **2013**, *7*, 9724–9734.
36. Banerjee, A.; Bhatia, D.; Saminathan, A.; Chakraborty, S.; Kar, S.; Krishnan, Y. Controlled Release of Encapsulated Cargo from a DNA Icosahedron Using a Chemical Trigger. *Angew. Chem., Int. Ed.* **2013**, *52*, 6854–6857.
37. Karanth, H.; Murthy, R. S. R. pH-Sensitive Liposomes—Principle and Application in Cancer Therapy. *J. Pharm. Pharmacol.* **2007**, *59*, 469–483.
38. Kaliss, N.; Pressman, D. Plasma and Blood Volumes of Mouse Organs, As Determined with Radioactive Iodoproteins. *Exp. Biol. Med.* **1950**, *75*, 16–20.